Journal of Solid State Chemistry 314 (2022) 123426

Contents lists available at ScienceDirect

Journal of Solid State Chemistry

journal homepage: www.elsevier.com/locate/jssc

Structural and dielectric properties of ultra-fast microwave-processed $La_{0.3}Ca_{0.7}Fe_{0.7}Cr_{0.3}O_{3-\delta}$ ceramics

Elena Sánchez-Ahijón [a], Rainer Schmidt [b], Xabier Martínez de Irujo-Labalde [c], Haris Masood Ansari [d,e], María Teresa Fernández-Díaz [f], Emilio Morán [a], Beatriz Molero-Sánchez [e], Jesús Prado-Gonjal [a,*]

[a] Dpto. Química Inorgánica, Universidad Complutense de Madrid, E-28040 Madrid, Spain
[b] GFMC, Dpto. de Física de Materiales, Facultad de Ciencias Físicas, Universidad Complutense de Madrid, E-28040 Madrid, Spain
[c] Department of Chemistry, Inorganic Chemistry Laboratory, University of Oxford, Oxford OX1 3QR, UK
[d] Department of Chemistry, University of Calgary, Calgary, Alberta T2N 1N4, Canada
[e] SeeO2 Energy Inc, 3655 36, St NW, Calgary, AB T2L 1Y8, Canada
[f] Institut Laue Langevin, BP 156X, Grenoble F, 38042, France

ARTICLE INFO

Keywords:
Microwave synthesis
Microwave sintering
Perovskite
Reversible Solid Oxide Fuel Cells
Neutron Powder Diffraction
Impedance spectroscopy

ABSTRACT

Perovskite $La_{0.3}Ca_{0.7}Fe_{0.7}Cr_{0.3}O_{3-\delta}$ (LCFCr) is a mixed ionic and electronic conductor (MIEC) that can be employed as an electrode material in reversible solid oxide fuel cells (RSOFCs). In this work, an ultra-fast (15 min) one-step microwave (MW)-assisted combustion synthesis route has been developed to obtain phase pure and highly crystalline LCFCr powder. The synthesized powders exhibited a sponge-like microstructure with increased electrochemical reaction sites. Neutron thermodiffraction analysis revealed a structural transition above 500 °C from the room temperature (RT) orthorhombic *Pnma* to a rhombohedral *R3c* perovskite phase. The oxygen vacancy concentration was found to increase from $\delta = 0.272(7)$ at RT to $\delta = 0.333(5)$ at 900 °C. Furthermore, a 3-dimensional G-type antiferromagnetic structure was detected at RT. MW-sintering of pressed green ceramic pellets was carried out at 950 °C for 1 h, using a MW-transparent quartz fiber crucible or alternatively a SiC crucible acting as a MW-absorber. Impedance spectroscopy data on sintered ceramic pellets revealed electronic inhomogeneity as demonstrated by the occurrence of three dielectric relaxation processes associated with two grain boundary (GB)-like contributions and one bulk. The dielectric inhomogeneity encountered may be restricted to the extrinsic GB areas, which may be rather thin. More homogeneous dielectric properties of the GBs were found in the pellet that was sintered in the SiC crucible.

1. Introduction

Reversible solid oxide fuel cells (RSOFCs) with operating temperatures in the range of 800–1000 °C have attracted considerable research attention in recent years due to potential application in the energy sector for the storage and timely release of energy that has been harvested by intermittent renewable energy sources such as wind and solar [1–3]. Similar to batteries, these devices can operate either in the Solid Oxide Fuel Cell (SOFC) mode to deliver electricity (and heat) or in the Solid Oxide Electrolysis Cell (SOEC) mode to store energy in the form of chemically stable gases. SOFCs convert H_2 and O_2 to H_2O, clean electricity and heat at high efficiencies, whereas SOECs electrolyze H_2O to H_2 and O_2, or co-electrolyze $CO_2 + H_2O$ to form syngas ($H_2 + CO$) and O_2 (Fig. 1). In fact, CO_2 or $CO_2 + H_2O$ electrolysis is thermodynamically and kinetically favorable if carried out at high temperature [3,4].

Most of the current research in RSOFCs is based on the state-of-the-art of SOFCs [5] and SOECs, where gadolinium-doped ceria (GDC) or Yttria-stabilized zirconia (YSZ) are typical electrolyte materials, whereas Ni-YSZ, Cu–CeO_2 or doped $SrTiO_3$ can act as fuel electrodes [1,6–15]. As an oxygen electrode material, perovskite $La_{1-x}Sr_xCo_{1-y}M_yO_{3-\delta}$ (M = transition metal) has been proposed as a promising candidate [16], but certain drawbacks exist. The Sr cations can segregate through the structure, reacting with other components of the cell and producing cell degradation, and in some occasions the ionic conductivity is poor at low temperatures [17,18]. Other interesting perovskite oxygen electrode materials have been reported, such as Co-based $Ba_{0.5}Sr_{0.5}Co_{0.8}Fe_{0.2}O_{3-\delta}$,

* Corresponding author.
E-mail address: jpradogo@ucm.es (J. Prado-Gonjal).

https://doi.org/10.1016/j.jssc.2022.123426
Received 7 June 2022; Received in revised form 7 July 2022; Accepted 10 July 2022
Available online 13 July 2022

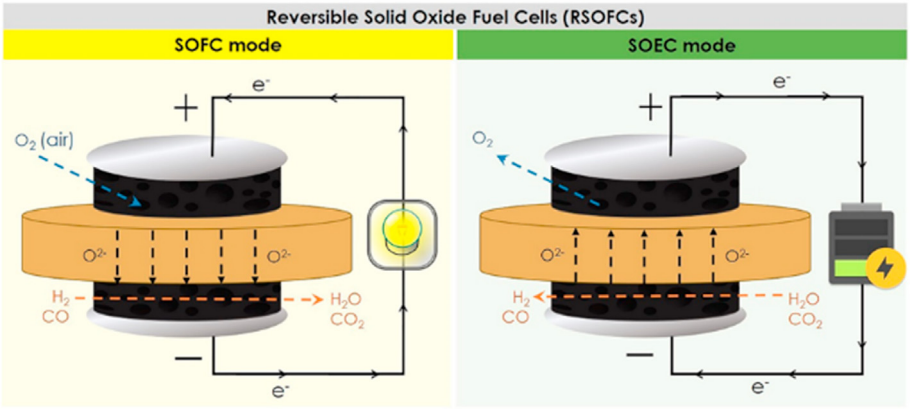

Fig. 1. Schematic drawing of the basic functionality of Reversible Solid Oxide Fuel Cells (RSOFCs) in both SOFC and SOEC modes.

$BaCo_{0.8}Zr_{0.1}Y_{0.1}O_{3-\delta}$, $La_{0.8}Ca_{0.2}CoO_{3-\delta}$, and $SmSrCo_{2-x}Mn_xO_{5+\delta}$ [19–21]. It should be noted at this point that the terms fuel and oxygen electrodes refer to the anode and cathode materials, respectively, when operating in SOFC mode and vice versa in SOEC mode.

Although Co-based perovskites show high catalytic activity for oxygen reduction reactions (ORRs) at intermediate temperatures, the presence of Co compromises the chemical stability of the cell. Furthermore, the high redox activity of Co is responsible for large thermal expansion coefficients (TECs), affecting the long-term stability of the cell [17,22].

Therefore, the Co-free orthorhombic perovskite phase $La_{0.3}Ca_{0.7}Fe_{0.7}Cr_{0.3}O_{3-\delta}$ (LCFCr) has been proposed as an ideal alternative, since it is structurally and chemically stable over a wide pO_2 range (0.21 atm–10^{-20} atm) and shows excellent electrochemical activity towards both ORRs and oxygen evolution reactions (OERs) [23]. This LCFCr phase and similar variants like $La_{0.3}Sr_{0.7}Fe_{0.7}Cr_{0.3}O_{3-\delta}$ (LSFCr) had been reported previously as potential materials for single or mixed anodes in SOFCs, in pure form or dispersed in Gd-doped ceria (GDC) $Gd_xCe_{1-x}O_{2-x/2}$ [24–27]. These phase compositions brought forward in references [24–27] were in fact modifications of materials like $La_{0.2}Sr_{0.8}Fe_{0.8}Cr_{0.2}O_{3-\delta}$ and $La_{0.2}Ca_{0.8}CrO_{3-\delta}$ that had been reported already many decades ago as potential catalysts for methane SOFC mixed anodes [28,29].

After it became clear that LCFCr may be a highly promising electrode material for RSOFCs, the compound was investigated more comprehensively. First, LCFCr was shown to exhibit thermomechanical stability, favorable oxygen transport kinetics and excellent electrochemical activity towards ORRs and OERs in symmetrical LCFCr/GDC/LCFCr cells with a low polarization resistance (R_p) of 0.07 Ω cm^2 at 800 °C in open-circuit conditions [23]. Subsequently, such findings were confirmed in LCFCr/GDC/YSZ/GDC/LCFCr symmetrical cells with excellent electrochemical performance towards CO oxidation (SOFC mode) and CO_2 electrolysis (SOEC mode) [30]. Such properties were further confirmed in a 3-electrode half-cell, where a thickness of 43 μm of porous screen-printed LCFCr electrodes was found to give the best cell performance as well as a low polarization resistance of ≈0.06–0.07 Ω cm^2 at 800 °C [31].

Since all such results indicated that LCFCr may be highly relevant for application in industrial environments [32], advanced energy saving synthesis routes have been employed to reduce the potential production costs. Initially, the material was synthesized by combustion synthesis involving the dissolution of precursor nitrates, adding glycine as a fuel and auto-igniting the combustion during conventional heating, followed by an additional calcination step at 1200 °C for 12 h in a conventional furnace [23]. As a step forward, microwave(MW)-assisted combustion and MW-assisted sol-gel synthesis routes have been explored [33,34]. The former route involved MW irradiation at 800 W for 30 min of the precursor nitrates and glycine mixture to auto-ignite the combustion process, followed by a second calcination step at 900 °C for 6 h. The latter route involved forming a gel by adding polyvinyl-alcohol (PVA) to the dissolved precursor nitrates, followed by heating at 80 °C for 1.5 h. The gel was MW-irradiated at 800 W for 30 min, followed by a second calcination step at 1000 °C for 6 h.

Since the MW-assisted combustion technique seemed to offer higher time and energy savings, it has been further developed here in this work. The mixture of precursor nitrates and glycine was MW-heated at 800 W for only 15 min to auto-ignite the combustion process and complete the chemical reaction. Most likely due to an improved experimental setup, the desired LCFCr phase was obtained reproducibly in highly crystalline and pure form without a second calcination step. It should be emphasized that this synthesis route presented here offers massive energy savings as compared to the routes reported previously and may, thus, be highly relevant for industrial applications, where energy costs are an important issue [35–38]. Furthermore, MW-sintering of pressed green ceramic bodies was carried out at 950 °C for 1 h at 1200 W, and highly dense ceramics were obtained. It was shown that the use of a SiC crucible acting as a MW-absorber [39] during MW-sintering (hybrid MW-sintering) of the ceramics leads to more homogeneous samples as compared to ceramics sintered in a MW-transparent quartz crucible (direct MW-sintering).

The LCFCr powders obtained here by the ultra-fast MW-combustion synthesis route were analyzed comprehensively by standard XRD and SEM, in addition to temperature dependent Neutron Powder Diffraction (NPD) experiments, whereas the sintered ceramic pellets were analyzed by temperature dependent impedance spectroscopy. The NPD and impedance spectroscopy measurement techniques have not been employed previously to LCFCr materials, thus, leading to unprecedented insights into the temperature dependent crystallographic structure, the magnetic structure, and the temperature dependent dielectric properties of this compound.

The results from Rietveld refinements of the NPD patterns indicated a temperature dependent concentration of oxygen vacancies and a gradual orthorhombic to rhombohedral structural transition upon heating above 500 °C. Furthermore, a rearrangement of the oxygen vacancies to a more isotropic scenario was detected, which can be expected to be beneficial for the vacancy mobility and ionic conductivity.

Impedance spectroscopy data from sintered ceramics revealed clear correlations between the electronic charge transport properties and the orthorhombic to rhombohedral structural transition. Furthermore, the use of the SiC crucible (hybrid MW-sintering) was shown to lead to electronically more homogeneous samples.

2. Experimental

2.1. Synthesis

$La_{0.3}Ca_{0.7}Fe_{0.7}Cr_{0.3}O_{3-\delta}$ was synthesized by an ultra-fast one-step MW

assisted-combustion route. The stoichiometric amounts of metal nitrate precursors [$La(NO_3)_3{\cdot}6H_2O$, Sigma-Aldrich, 99%; $Ca(NO_3)_2{\cdot}4H_2O$, Sigma-Aldrich, 99.997%; $Fe(NO_3)_3{\cdot}9H_2O$, Sigma-Aldrich, 98%; $Cr(NO_3)_3{\cdot}9H_2O$, Sigma-Aldrich, 99%] to form 10 g of the product were mixed and dissolved in a minimum amount of deionized water. Once the nitrates were fully dissolved, the solution was mixed with 2 mol of glycine for each mol of metal nitrate. The mixture was placed into a porcelain capsule that is transparent to MWs and no MW absorption was expected. On the other hand, the high polarity of the water solvent, the nitrate groups and their water of hydration leads to efficient and direct absorption of the MW energy within the precursors. The porcelain crucible was placed into a domestic microwave furnace (Proclean 3010, Cedotec) at 2.45 GHz and 700 W for 15 min (Fig. 2a) to perform MW-assisted combustion synthesis. The mixture auto-ignites during the MW irradiation, the combustion process initiates, and the precursors chemically react to form a black and porous highly crystalline and phase pure LCFCr powder.

2.2. Sintering

The LCFCr powders were pressed into green body pellets using an uniaxial 2 ton die press for 5 min with a nominal diameter of 10 mm and a thickness of around 2 mm. The green bodies were placed into a quartz fiber crucible, transparent to MWs (direct MW-sintering), or into a SiC crucible acting as a MW absorber (hybrid MW-sintering), as depicted schematically in Fig. 2b.

The MW-sintering processes were carried out in a commercial MW furnace (Milestone MultiFAST-6 MW accessory coupled to the Milestone Ethos One instrument). A heating ramp of 35 °C/min was applied and the ceramics were sintered at 950 °C for 1 h.

The density of the ceramic pellets after direct MW-sintering was ≈ 87%, while the hybrid MW-sintering resulted in a slightly increased density of ≈ 90%. Both densities were regarded sufficiently high for reliable impedance spectroscopy measurements.

2.3. Structural and microstructural characterization

Powder NPD data from RT to 900 °C were collected at the D2B beamline at the Institut Laue Langevin (ILL), Grenoble. A wavelength of 1.549 Å was used in the 2θ angular range of 5–150°. Considering the difference in the neutron scattering lengths of the constituent elements in the LCFCr sample, this experiment allowed determining the oxygen content and the possible cation ordering in the structure. NPD data were collected at RT during 3 h for a 3 g sample, packed in a cylindrical vanadium can, in the high-intensity mode. Furthermore, NPD patterns were also collected for 3 h at 300 °C, 500 °C, 800 °C and 900 °C. In these cases, the powders were measured in a quartz-tube open to air.

Fullprof software [40] was employed for refining the structure from the NPD data. Pseudo-Voigt functions were used to adjust the shape profile, while scale factor, manual background, zero-point error, asymmetry, cell parameters, atomic positions, occupancy of the elements and isotropic atomic displacement parameters were refined. In the case of the

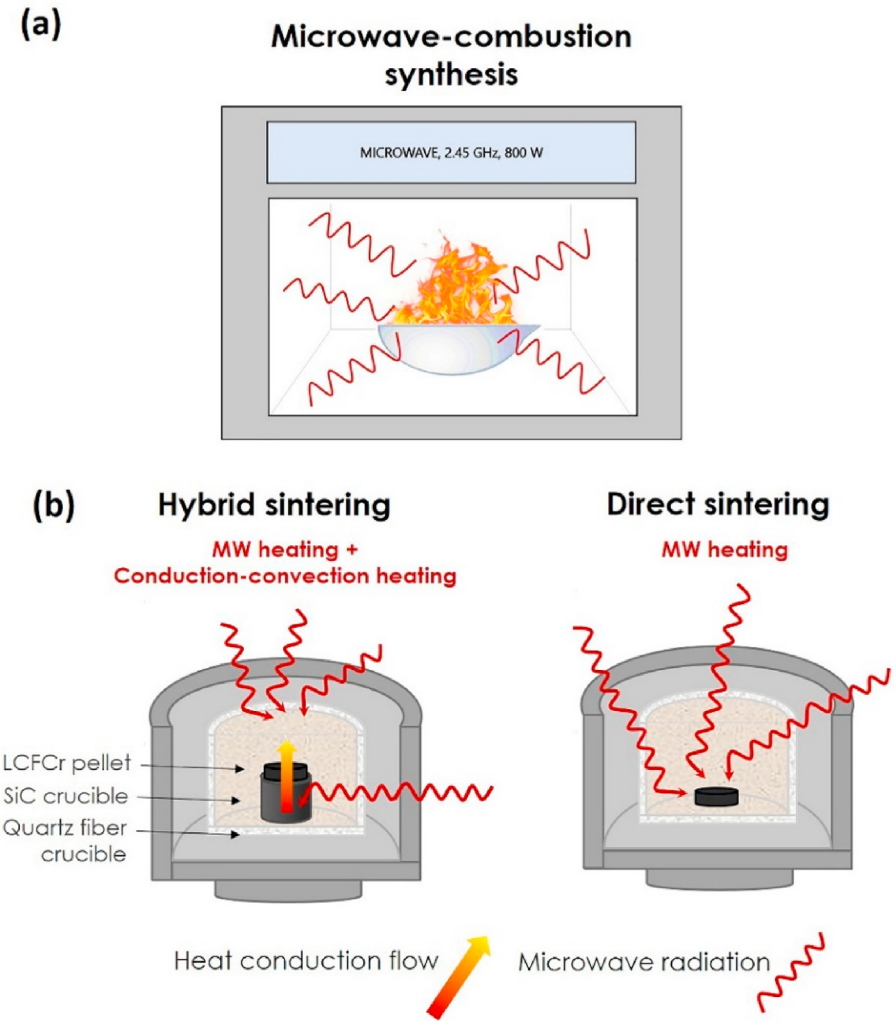

Fig. 2. Schematics of (a) Microwave-combustion synthesis and (b) Microwave-sintering showing the two sintering modes: Hybrid MW- and direct MW-sintering.

data collected at RT, the magnetic structure was refined by using the BasIreps program [41].

The microstructure of the powder and pellets were examined by scanning electron microscopy (SEM) on a JEOL 6400 microscope equipped with a detector for energy-dispersive analysis of X-rays (EDAX).

Thermogravimetric analysis (TGA) of a 30 mg powder sample was carried out in a Q600 TA Instruments from RT to 900 °C in air and in N_2, using a heating rate of 5 °C/min.

2.4. Impedance spectroscopy on MW-heated pellets

Impedance spectroscopy was carried out on sintered ceramic pellets using both the direct MW-heating and the hybrid MW-heating methods. Au electrodes were sputter deposited onto the pellet surfaces and covered with Ag quick-drying paint. Impedance data were collected using a Novocontrol Alpha-A High Performance Frequency analyzer, equipped with a liquid nitrogen cooled sample chamber. The data were measured at steady state conditions between 160 and 500 K, where each temperature (T) was allowed to stabilize for at least 10 min before measuring the impedance. The applied alternating voltage signal had a 100 mV amplitude and was applied over a frequency (f) range of 1 Hz–10 MHz. The impedance data were measured in terms of the f and T dependent real and imaginary parts of the complex impedance $Z^* = Z' + iZ''$. The data were converted into the format of dielectric permittivity ε' using the standard conversion. The data were analyzed and plotted using commercial Microsoft Excel® spreadsheets developed by SSSS® and were fitted with Zview® software [42].

3. Results and discussion

3.1. Neutron powder diffraction

Fig. 3 shows the neutron diffraction data collected at RT. Although the sample is synthesized within only 15 min, high crystallinity and phase purity are observed. This confirms that the MW-assisted combustion synthesis route presented here offers massive time and energy savings without compromising on the sample quality.

$La_{0.3}Ca_{0.7}Fe_{0.7}Cr_{0.3}O_{3-\delta}$ was reported to crystallize in a perovskite structure with an orthorhombic *Pnma* space group and $\sqrt{2}a_p x 2a_p x \sqrt{2}a_p$ unit cell dimensions (p denotes the cubic perovskite structure) [23]. Rietveld refinements of the NPD data collected at RT confirm the long-range periodic crystal structure (Fig. 3) and give some insights about the cation and anion sublattices. Table 1 contains the calculated cell parameters, crystallographic positions and fitted values obtained from the refinements. Both, A- and B- site cations are randomly distributed within the structure. An oxygen deficiency of $\delta = 0.272(7)$ was detected, which leads to an average oxidation state for the B-site cations of +3.16, which is near the preferable Fe^{3+} and Cr^{3+} cation oxidation states.

Interestingly, oxygen vacancies are located only in the O2 crystallographic sites, indicating a 2D arrangement. Since Cr^{3+} has a strong propensity for octahedral oxygen coordination, oxygen vacancies would preferentially be located around the Fe^{3+} cation. Fe^{3+} has a d^5 electronic configuration, which may be more flexible to adopt to different oxygen coordination numbers. In related compounds such as $LaCa_2Fe_3O_8$ or $Ca_2Fe_2O_5$ [43,44], some Fe cations situated in particular layers exhibit a tetrahedral oxygen coordination, which may well be the case in $La_{0.3}Ca_{0.7}Fe_{0.7}Cr_{0.3}O_{3-\delta}$, too. The tetrahedral oxygen coordination may explain the localization of the associated oxygen vacancy on the O2 sites to some extent, whereby the tetrahedra would be randomly distributed within the structure, at least on average. An oxygen content of $\delta = 0.33$ would require Fe cations to be surrounded by oxygen octahedra and tetrahedra in a 1:1 ratio. Since the oxygen deficiency observed is slightly lower, Fe is thus expected to be surrounded by more oxygen octahedra as compared to tetrahedra. These additional Fe in octahedral coordination would suggest a higher oxidation state, which is consistent with the extra charge of +3.16 obtained.

The high atomic displacement parameters (B_{iso}) observed in both the O1 and O2 crystallographic positions may well be associated with a random distribution of the Fe tetrahedra and the associated oxygen vacancies within the layers, but also with the different oxygen environments around the Fe and Cr cations.

Fig. 4 shows the NPD data collected between RT and 900 °C. Structural details of the Rietveld refinement of the NPD data collected at 300 °C, 500 °C and 800 °C are shown in the Electronic Supplementary Information.

The amorphous signal at low 2θ (from 300 °C to 900 °C) corresponds to the quartz sample container. The data in Fig. 4 demonstrate that two sets of reflections disappear as the temperature increases. Due to the few temperatures where NPD data was taken, the resolution of the phase transition temperature is somewhat limited. The first reflection (green bar in Fig. 4b) may disappear at or slightly above ≈ 300 °C, whereas the second reflection (blue bar in Fig. 4b) is still present at 500 °C but absent at 800 °C. The two apparent phase transitions at ≈ 300 °C - 500 °C and ≈ 500 °C - 800 °C are discussed in the following. The high temperature phase transition may in fact set in already at ≈ 500 °C, because the

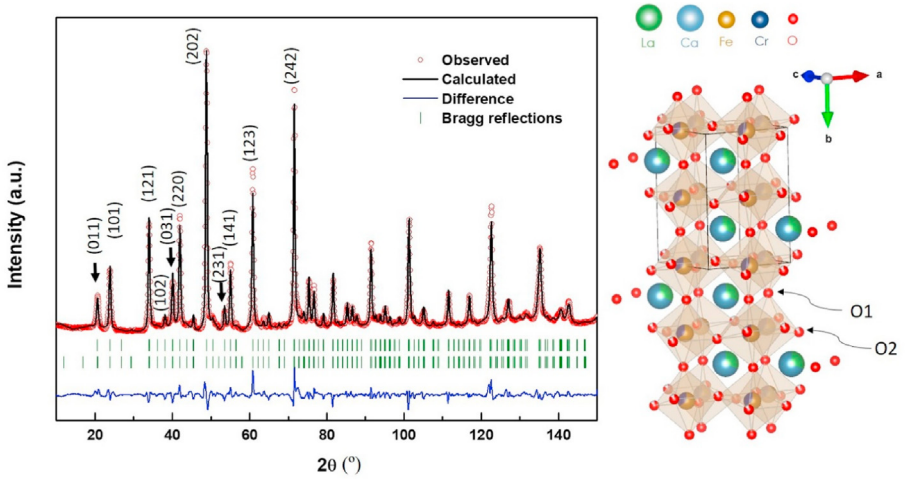

Fig. 3. Rietveld Refinement of NPD data for $La_{0.3}Ca_{0.7}$ $Fe_{0.7}Cr_{0.3}O_{3-\delta}$ collected at RT. Observed (red) and calculated (black) profiles, and their difference (blue) are shown. The upper and lower tick marks in green indicate the nuclear and magnetic reflections, respectively. Black arrows indicate the most intense magnetic reflections. The crystal structure obtained from the Rietveld refinement data is shown in the right part of the figure O1 and O2 positions are indicated.

Table 1
Results of the Rietveld Refinement of the crystal structure of $La_{0.3}Ca_{0.7}Fe_{0.7}Cr_{0.3}O_{3-\delta}$ from NPD data collected at RT.

Atom	Wyckoff	*x*	*y*	*z*	B_{iso} (Å^2)	Occupancy (%)
La/Ca	4*c*	0.012(1)	0.25	0.996(2)	1.334(2)	28.6(8)/71.4(8)
Fe/Cr	4*b*	0	0	0.5000	0.37(7)	62.6(8)/37.4(8)
O1	4*c*	0.006(1)	0.25	0.463(1)	1.5(1)	100
O2	8*d*	0.281(1)	0.0382(7)	0.717(1)	1.78(8)	86.1(7)

Pnma; $a = 5.4501(4)$ Å, $b = 7.7089(5)$ Å, $c = 5.4607(4)$ Å
$R_{wp} = 5.73\%$, $R_p = 4.41\%$, $R_{exp} = 1.22\%$, $R_B = 4.54\%$

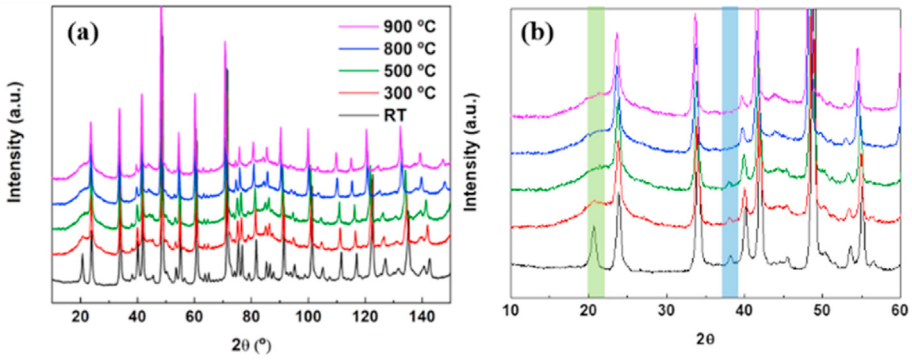

Fig. 4. (a) NPD data for $La_{0.3}Ca_{0.7}$ $Fe_{0.7}Cr_{0.3}O_{3-\delta}$ collected from RT to 900 °C and (b) enlarged details for 2θ diffraction angles of $10° < 2\theta < 60°$. Two phase transitions are highlighted by the green and blue bars. The irregular background above RT comes from the quartz container used for data collection, permitting the sample to be in contact with air at high temperatures.

relevant NPD peak in the blue bar in Fig. 4b is already weakened. Across the phase transition, the respective Rietveld refinements indicate a change from orthorhombic *Pnma* to rhombohedral *R3c* crystal symmetry, where the latter may in fact be equivalent to the *R-3c* phase in the related $La_{0.3}Sr_{0.7}Fe_{0.7}Cr_{0.3}O_{3-\delta}$ compound [27]. Fig. 5 and Table 2 show the Rietveld refinement and the structural representation of LCFCr at 900 °C. The evolution of the oxygen content with temperature and the structural parameters are presented in the Electronic Supplementary Information. It can be observed that the atomic displacement parameters (B_{iso}) are large. This is related to the increment of thermal vibrations and dynamic positional disorders of the elements at high temperature.

The oxygen content is slightly lower at 900 °C ($\delta = 0.333(5)$) as compared to RT ($\delta = 0.272(7)$), which might be associated with the reduction of Fe^{4+} to Fe^{3+}. Generally, the change in the distribution of the oxygen vacancies to a more isotropic scenario at and above 800 °C and the variation in oxygen content with temperature indicate a considerable

Table 2
Results of the Rietveld Refinement of the crystal structure of $La_{0.3}Ca_{0.7}Fe_{0.7}$-$Cr_{0.3}O_{3-\delta}$ from NPD data at 900 °C.

Atom	Wyckoff	*x*	*y*	*z*	B_{iso} (Å^2)	Occupancy (%)
La/Ca	6*a*	0	0	0.25	3.34(8)	28.6/71.4
Fe/Cr	6*a*	0	0	0.988(1)	1.58(3)	62.6/37.4
O1	18*b*	0.128(1)	0.306(2)	0.095(2)	3.66(9)	88.9(5)

R3c; $a = 5.5130(3)$ Å, $c = 13.4866(9)$ Å
$R_{wp} = 3.77\%$, $R_p = 2.78\%$, $R_{exp} = 1.77\%$, $R_B = 5.38\%$

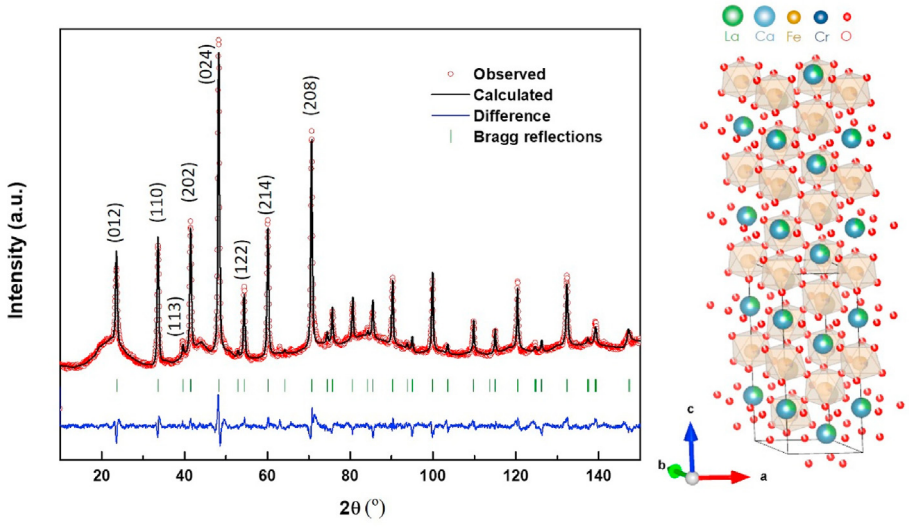

Fig. 5. Rietveld Refinement of the NPD data for $La_{0.3}Ca_{0.7}$ $Fe_{0.7}Cr_{0.3}O_{3-\delta}$ collected at 900 °C. Observed (red) and calculated (black) profiles and their difference (blue) are shown. The structure of the perovskite phase obtained from the Rietveld refinement data is shown in the right part of the figure.

mobility of the oxygen vacancies, which may well be beneficial for the ionic charge transport. The decrease in oxygen content is consistent with the thermogravimetric analysis (TGA) results (see Electronic Supplementary Information), which confirm the weight loss during heating and the associated oxygen loss. The second transition at ≈ 300 °C may be associated to magnetic ordering around 300 °C. A relationship between the magnetic and structural transitions is not indicated from the data acquired here in this work, although it cannot be discarded. The magnetic reflections lie on the same position as the nuclear ones, which suggests a propagation vector k = [0 0 0], or in other words, both the magnetic and nuclear structures present the same dimensions ($\sqrt{2}a_p x 2a_p x \sqrt{2}a_p$). Analysis of the irreproducible representations suggests a 3-dimensional G-type antiferromagnetically ordered arrangement of the spins, orientated along the long *a* axis. A representation of the magnetic structure is shown in Fig. 6.

At RT, an average magnetic moment of 1.52(3) μB for Fe and Cr cations was determined, while the calculated magnetic moment would result in μ = (0.7x5μB-0.3x3μB) = 2.5 μB, which is higher than the experimental value obtained. This may be ascribed to several possible factors such as a certain degree of disorder in the competing ferro- and anti-ferromagnetic interactions, thermal spin fluctuations at 300 K, the extra electron charge observed in some of the Fe cations to compensate oxygen vacancies and a perceptible covalent character of the bonding between the transition metals and oxygen on tetrahedral Fe sites.

3.1.1. Scanning electron microscopy (SEM)

A sponge-like microstructure of the MW ultra-fast synthesized LCFCr powder can be observed from the SEM micrograph shown in Fig. 7a. This is essential for RSOFC electrodes, because porosity helps maximizing the number of electrochemical reactions sites and improves the gas diffusion rate to enhance electrochemical performance. The powder microstructure presented here is typical for phases obtained from combustion processes. It should be noted here that the phase obtained was highly crystalline, which is not always the case in combustion processes [45]. The observed porosity may be ascribed to the exothermic reaction occurring during combustion, which leads to the generation and expulsion of gases such as CO_2, N_2, and H_2O. This in turn leads to the formation of pores and an increased specific surface area of the material.

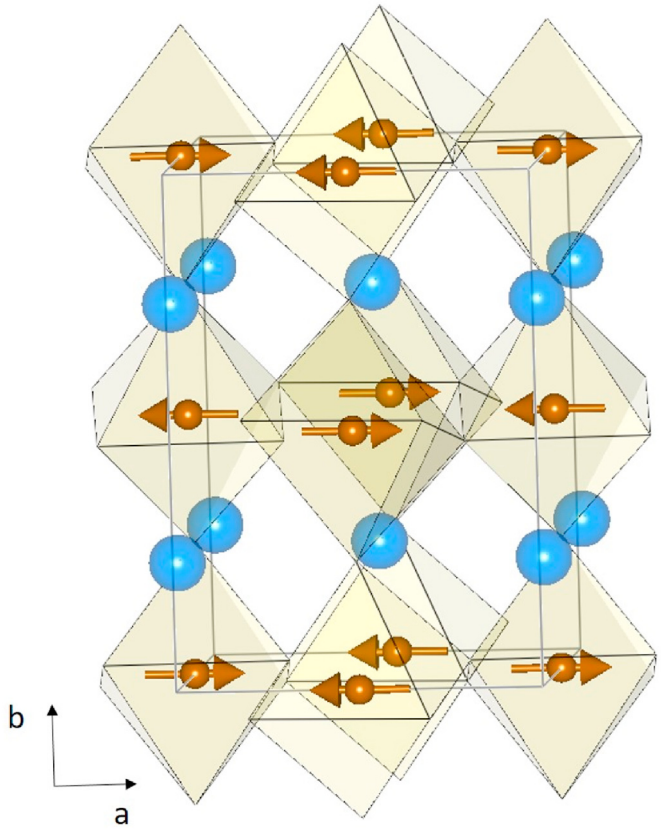

Fig. 6. Magnetic structure of $La_{0.3}Ca_{0.7}Fe_{0.7}Cr_{0.3}O_{3-\delta}$ at RT.

This may be regarded a major advance, because in conventional combustion synthesis a second calcination process is necessary to obtain crystalline material, whereby the high degree of porosity often disappears or is diminished considerably. The ultra-fast MW synthesis route developed here allows the fabrication of highly crystalline and phase pure material, without compromising on the high level of porosity. Fig. 7b and c shows the microstructure of the sintered pellets using the direct and hybrid MW-sintering processes, respectively. No significant differences in the morphology of the samples were detected and the samples were considered to be sufficiently dense for reliable impedance spectroscopy measurements.

3.2. Impedance spectroscopy of sintered pellets

Impedance spectra collected from a pellet sintered by the direct MW-sintering method are presented in Fig. 8 shown in different formats. Fig. 8a displays the data in the format of the real part of the impedance Z' vs f, where the open symbols correspond to the data and the solid lines and full circles represent the curves that were fitted to the data by applying the equivalent circuit model depicted in Fig. 8b.

The low-f limit shown in Fig. 8a in form of an f-independent plateau corresponds to the direct current (DC) limit. At low T of 160–180 K, the two clearly distinct plateaus in Fig. 8a can be assigned to two distinct dielectric contributions of extrinsic grain boundary (GB) and intrinsic bulk, as indicated. Due to the high conductivity or low resistivity, the intrinsic bulk contribution is clearly visible only at low $T < 200$ K, where the conduction process is sufficiently slow. The extrinsic GB contribution is the dominant contribution in terms of the electrical resistivity and, therefore, dominates the impedance data plotted in the format of Z'' vs Z' in Fig. 6b, which displays one main asymmetric semicircle. The diameter of the semicircle is a measure of the resistivity of the GBs at the respective $T = 160$ K, whereas the asymmetry is a manifestation of the occurrence of in fact two similar and overlapping GB contributions. These two GB dielectric contributions can only be fitted satisfactorily with two non-ideal RC elements, where the ideal capacitor had been replaced by a constant-phase element (CPE) to account for the dielectric non-ideality in terms of a certain distribution of the dielectric relaxation times τ [46,47].

The presence of two similar GB dielectric contributions implies that the extrinsic GBs are dielectrically not uniform, which may well be explained by the ultra-fast MW synthesis and the direct MW-sintering processes that both occur far away from thermodynamic equilibrium. This dielectric inhomogeneity had not been reflected though in the microstructural characterization of the sintered pellets in section 3.2. using SEM, and neither in the structural analysis in section 3.1. using NPD. This suggest that the dielectric inhomogeneity encountered may be restricted to the extrinsic GB areas, which may be rather thin. The stoichiometric differences between the different GB dielectric contributions would be restricted to such small areas and may thus not be detectable in the standard structural data. The microstructural differences between the two different types of GBS may be small, since no clear difference can be observed by SEM.

The equivalent circuit model used for impedance spectroscopy data fitting consists of a total of 3 non-ideal R-CPE elements in series, one for the bulk and two for the GB contributions, where good agreement between data and model is indicated in Fig. 8a and b. The resistivity ρ values extracted from the equivalent circuit model for the bulk (R1) and the two GB contributions (R2 & R3) are plotted on a log-scale vs $1/T$ in Fig. 6c, together with a plot of the real part of the impedance log (Z') at 1 Hz vs $1/T$, which corresponds to the low-f plateau in the Z' vs f curves in Fig. 6a. As mentioned before, this plateau can be interpreted as the DC resistivity limit and gives thus a reliable picture of the DC resistivity. All

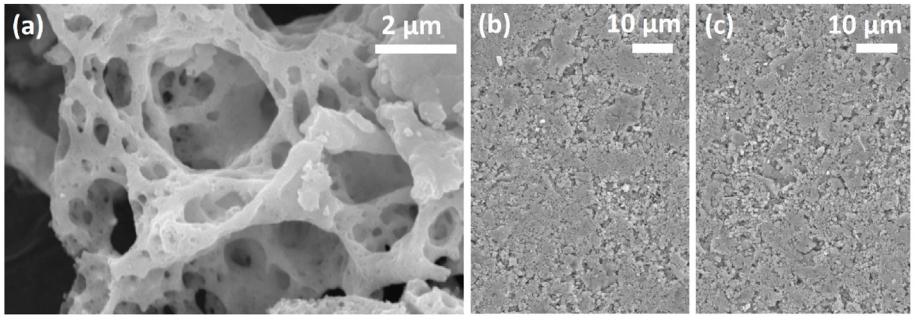

Fig. 7. SEM micrographs of LCFCr: (a) powder, (b) pellet sintered by the direct MW process, (c) pellet sintered by the hybrid MW process using SiC crucible as a microwave susceptor.

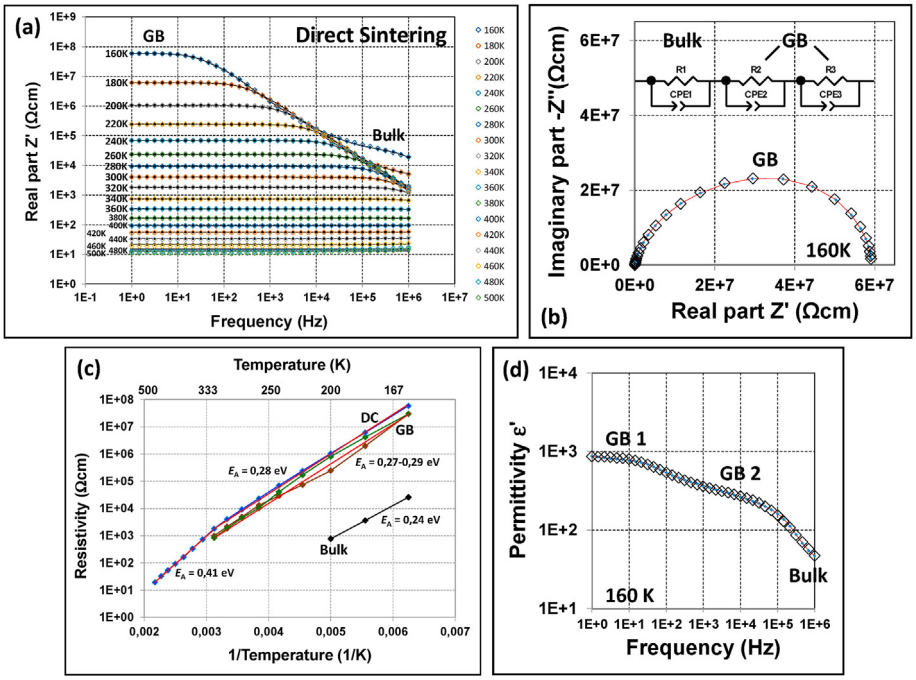

Fig. 8. Impedance spectroscopy data for a direct MW-sintered ceramic in the formats of **(a)** Z' vs f, and **(b)** Z'' vs Z'. The figure inset shows the equivalent circuit model, **(c)** log(ρ) vs $1/T$ extracted from the equivalent circuit fits, where the continuous lines are guide to the eyes to indicate good linearity, and **(d)** ε' vs f. Open symbols correspond to the data and solid lines and full symbols represent the curves fitted to the equivalent circuit model.

curves in Fig. 6c exhibit reasonable linearity, which indicates semiconducting thermally activated charge transport. The bulk resistivity ρ is considerably smaller than the GB resistivity, which implies that the GBs act as barriers for the electronic charge transport. Still, the resistivity is generally rather low, especially at higher T, and the material may be regarded sufficiently conducting for potential application as an electrode in reversible SOFCs. From the slopes of the corresponding Arrhenius plots of ln(ρ) vs $1/T$ (not shown here), the activation energies E_A were determined to be $E_A = 0.24$ eV for the bulk and in the range of $E_A = 0.27$–0.29 eV for the two GB contributions. The DC resistivity is dominated by the two GB contributions and exhibits an activation energy of $E_A = 0.28$ eV at low and intermediate T. At higher T, the two GB contributions cannot be distinguished and can be fitted with one R-CPE element only (data not shown), where the log(ρ) vs $1/T$ curve would be practically identical with the DC curve. It is important to note that the DC curve shows clear transitional features near 320 K and displays a higher activation energy of $E_A = 0.41$ eV above ≈320 K. This obvious transition at ≈ 320 K may well be correlated with the magnetic transition observed in the NPD data at ≈ 300 K.

The two distinct GB contributions can be identified most clearly by plotting the data in the format of the real part of the dielectric permittivity ε' vs f in Fig. 8d. At low and intermediate f, two distinct permittivity plateaus can be identified, which can be associated with the two GB contributions. The rather high ε' values of the two plateaus allow the association of these contributions to an extrinsic origin, typical for GB dielectric contributions [46,48]. The bulk dielectric contribution cannot be resolved, because the ε' vs f curve does not fully relax towards the bulk permittivity plateau as a result of the high-f experimental limit of the impedance spectroscopy technique. In a rather crude extrapolation the bulk permittivity may be expected to be in the range of roughly $\varepsilon' \approx 40$.

Fig. 9a–d shows the equivalent data and fitted curves as in Fig. 8 but for a pellet that was MW-sintered by the hybrid method using SiC crucibles. Fig. 9a shows the plateau features of the DC limit at low f and the presence of two distinct dielectric contributions of bulk and GBs, equivalent to the pellet sintered by the direct sintering method.

The equivalent circuit applied was identical, and again, good agreement was displayed between data and the fitted curves shown in Fig. 9b. The main GB semicircle displayed in plots of Z'' vs Z' in Fig. 9b is slightly less asymmetric, which implies that the two GB contributions show rather similar time constants τ here, and the GB properties are dielectrically more homogeneous. The plots of log(ρ) vs $1/T$ in Fig. 9c display a slightly lower bulk activation energy $E_A = 0.22$ eV, and slightly lower GB activation

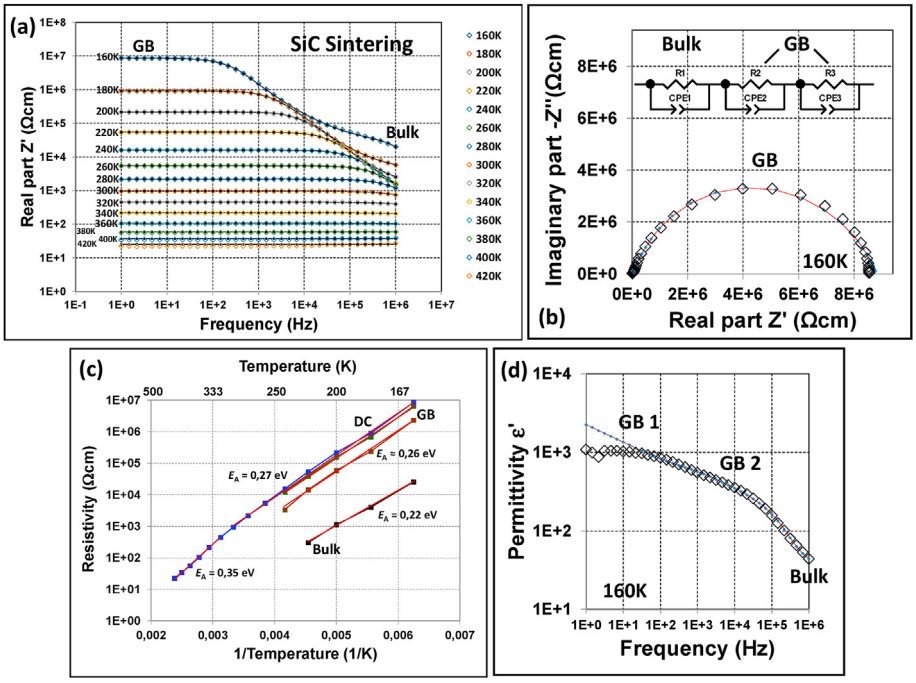

Fig. 9. Electrical impedance spectroscopy (EIS) data for a pellet that was treated by Hybrid Sintering in SiC crucibles. The data are displayed in the formats of **(a)** Z' vs f, **(b)** Z'' vs Z', the figure inset shows the equivalent circuit model, **(c)** $\log(\rho)$ vs $1/T$ extracted from the equivalent circuit fits, where the continuous lines are guide to the eyes to indicate good linearity, and **(d)** ε' vs f. Open symbols correspond to the data and solid lines and full symbols to the equivalent circuit fitted curves.

energies in the range of $E_A = 0.26$–0.27 eV. The transition at ≈ 320 K is less pronounced in the hybrid sintered pellet, where the DC activation energy $E_A = 0.35$ eV at high T is considerably lower here as compared to the direct MW-sintered pellet. The transition is more difficult to detect in the hybrid MW-sintered pellet and may in fact be less abrupt or more gradual. The two GB plateaus in the ε' vs f plots in Fig. 9d are less clearly pronounced as in Fig. 8d, confirming the dielectrically more homogeneous GB properties in the hybrid MW-sintered sample.

In a nutshell, although SEM micrographs and densities were very similar for both types of MW-sintered samples, perceptible differences in the dielectric properties were detected by impedance spectroscopy. The hybrid MW-heating might improve the temperature homogeneity across the pellet during sintering, and, therefore, the dielectric properties of the pellet would be more homogeneous.

4. Conclusions

Perovskite $La_{0.3}Ca_{0.7}Fe_{0.7}Cr_{0.3}O_{3-\delta}$ powder was synthesized by an ultra-fast one-step MW-assisted combustion process, offering massive time and energy savings. Pressed pellets were sintered by MW-assisted techniques. The temperature dependent powder NPD data revealed an orthorhombic *Pnma* to rhombohedral *R3c* phase transition upon heating, starting at ≈ 500 °C. The oxygen content decreases from $\delta = 0.272(7)$ at RT to $\delta = 0.333(5)$ at 900 °C. The magnetic structure of the sample was resolved at RT, showing 3-dimensional G-type antiferromagnetism. Impedance spectroscopy revealed two different grain boundary type (GB) dielectric contributions in the direct MW-sintered sample, where such inhomogeneity may be restricted to thin GB areas since it was not detectable in the standard structural and microstructural data. The occurrence of this dielectric inhomogeneity may still be regarded a confirmation that MW-heating processes occur far away from thermodynamic equilibrium that can lead to dielectric inhomogeneity. The two GB dielectric contributions were found to be more similar for hybrid MW-sintered ceramics.

CRediT authorship contribution statement

Elena Sánchez-Ahijón: Investigation, Writing – original draft. **Rainer Schmidt:** Conceptualization, Investigation, Methodology, Writing – review & editing. **Xabier Martínez de Irujo-Labalde:** Investigation, Writing – original draft. **Haris Masood Ansari:** Investigation. **María Teresa Fernández-Díaz:** Methodology, Resources. **Emilio Morán:** Conceptualization, Resources. **Beatriz Molero-Sánchez:** Conceptualization, Supervision, Investigation. **Jesús Prado-Gonjal:** Conceptualization, Investigation, Formal analysis, Funding acquisition, Supervision, Writing – review & editing.

Declaration of competing interest

The authors declare that they have no known competing financial interests or personal relationships that could have appeared to influence the work reported in this paper.

Data availability

No data was used for the research described in the article.

Acknowledgments

This work has been supported by the Madrid Government (Comunidad de Madrid- Spain) under the Multiannual Agreement with Complutense University in the line Program to Stimulate Research for Young Doctors in the context of the V PRICIT (Regional Programme of Research and Technological Innovation): Project *PR65/19–22459*. We thank to Spanish Ministry for Science and Innovation (MCIN/AEI/10.13039/501100011033) for granting the projects *PID2020-112848RB-C21* and *RTI2018-094550-A-I00*. We also wish to express our gratitude to the ILL and CNME technical staff for providing the facilities for neutron powder diffraction experiment and SEM, respectively.

Appendix A. Supplementary data

Supplementary data to this article can be found online at https://doi.org/10.1016/j.jssc.2022.123426.

References

[1] M. Asif, T. Muneer, Energy supply, its demand and security issues for developed and emerging economies, Renew. Sustain. Energy Rev. 11 (7) (2007) 1388–1413.

[2] J.G.E. Erdle, V.V. Meyringer, Possibilities for hydrogen production by combination of a solar thermal central receiver system and high temperature electrolysis of steam, Proceed. Third Int. Workshop 2 (1986) 727–736.

[3] C. Graves, S.D. Ebbesen, M. Mogensen, K.S. Lackner, Sustainable hydrocarbon fuels by recycling CO_2 and H_2O with renewable or nuclear energy, Renew. Sustain. Energy Rev. 15 (1) (2011) 1–23.

[4] C.W. Li, M.W. Kanan, CO2 reduction at low overpotential on Cu electrodes resulting from the reduction of thick Cu_2O films, J. Am. Chem. Soc. 134 (17) (2012) 7231–7234.

[5] E. Sánchez-Ahijón, R. Marín-Gamero, B. Molero-Sánchez, D. Ávila-Brande, A. Manjón-Sanz, M.T. Fernández-Díaz, E. Morán, R. Schmidt, J. Prado-Gonjal, From theory to experiment: $BaFe_{0.125}Co_{0.125}Zr_{0.75}O_{3-\delta}$, a highly promising cathode for intermediate temperature SOFCs, J. Mater. Chem. A 8 (6) (2020) 3413–3420.

[6] M.A. Yatoo, S.S. Kawale, S.J. Skinner, Perovskite and Layered Oxide Materials for Intermediate Temperature Solid Oxide Fuel Cells, Intermediate Temperature Solid Oxide Fuel Cells, Elsevier, 2020, https://doi.org/10.1016/B978-0-12-817445-6.00010-7.

[7] Y. Tian, W. Wang, Y. Liu, L. Zhang, L. Jia, J. Yang, B. Chi, J. Pu, J. Li, Cobalt-free perovskite oxide $La_{0.6}Sr_{0.4}Fe_{0.8}Ni_{0.2}O_{3-\delta}$ as active and robust oxygen electrode for reversible solid oxide cells, ACS Appl. Energy Mater. 2 (5) (2019) 3297–3305.

[8] M.E. Brito, H. Morishita, J. Yamada, H. Nishino, H. Uchida, Further improvement in performances of $La_{0.6}Sr_{0.4}Co_{0.2}Fe_{0.8}O_{3-\delta}$-doped ceria composite oxygen electrodes with infiltrated doped ceria nanoparticles for reversible solid oxide cells, J. Power Sources 427 (2019) 293–298.

[9] J. Prado-Gonjal, R. Heuguet, D. Muñoz-Gil, A. Rivera-Calzada, S. Marinel, E. Morán, R. Schmidt, Microwave synthesis & sintering of Sm and Ca co-doped ceria ceramics, Int. J. Hydrogen Energy 40 (45) (2015) 15640–15651.

[10] X. Hu, M. Li, Y. Xie, Y. Yang, X. Wu, C. Xia, Oxygen-deficient ruddlesden–popper-type lanthanum strontium cuprate doped with bismuth as a cathode for solid oxide fuel cells, ACS Appl. Mater. Interfaces 11 (24) (2019) 21593–21602.

[11] X.M. de Irujo-Labalde, D. Muñoz-Gil, E. Urones-Garrote, D. Ávila-Brande, S. García-Martín, Complex modulation of the crystal structure of a layered perovskite. A promising solid-oxide-fuel-cell cathode, J. Mater. Chem. A 4 (26) (2016) 10241–10247.

[12] N.Q. Minh, Reversible solid oxide fuel cell technology for hydrogen/syngas and power production, Hydr. Sci. Eng.: Mater. Proces. Sys. Technol. (2016) 359–390.

[13] D.W. Joh, J.H. Park, D. Kim, E.D. Wachsman, K.T. Lee, Functionally graded bismuth oxide/zirconia bilayer electrolytes for high-performance intermediate-temperature solid oxide fuel cells (IT-SOFCs), ACS Appl. Mater. Interfaces 9 (10) (2017) 8443–8449.

[14] W. Yang, T. Hong, S. Li, Z. Ma, C. Sun, C. Xia, L. Chen, Perovskite $Sr_{1-x}Ce_xCoO_{3-\delta}$ ($0.05 \leq x \leq 0.15$) as superior cathodes for intermediate temperature solid oxide fuel cells, ACS Appl. Mater. Interfaces 5 (3) (2013) 1143–1148.

[15] T. Mori, R. Buchanan, D.R. Ou, F. Ye, T. Kobayashi, J.-D. Kim, J. Zou, J. Drennan, Design of nanostructured ceria-based solid electrolytes for development of IT-SOFC, J. Solid State Electrochem. 12 (7) (2008) 841–849.

[16] N.Q. Minh, Development of reversible solid oxide fuel cells (RSOFCs) and stacks, ECS Trans. 35 (1) (2011) 2897.

[17] Y. Yamaguchi, I. Kagomiya, S. Minami, H. Shimada, H. Sumi, Y. Ogura, Y. Mizutani, $La_{0.65}Ca_{0.35}FeO_{3-\delta}$ as a novel Sr-and Co-free cathode material for solid oxide fuel cells, J. Power Sources 448 (2020), 227426.

[18] C. Berger, E. Bucher, C. Gspan, W. Sitte, Crystal structure, oxygen nonstoichiometry, and mass and charge transport properties of the Sr-free SOFC/SOEC air electrode material $La_{0.75}Ca_{0.25}FeO_{3-\delta}$, J. Solid State Chem. 273 (2019) 92–100.

[19] R.-W. You, J. Ouyang, Y.-P. Fu, S.-H. Hu, K.-W. Tay, Characterization of $Ce_{0.8}Sm_{0.2}O_{2-\delta}$-infiltrated $La_{0.8}Ca_{0.2}CoO_{3-\delta}$ cathode for solid oxide fuel cells, Ceram. Int. 39 (7) (2013) 8411–8419.

[20] Y. Wang, X. Zhao, S. Lü, X. Meng, Y. Zhang, B. Yu, X. Li, Y. Sui, J. Yang, C. Fu, Synthesis and characterization of $SmSrCo_{2-x}Mn_xO_{5+\delta}$ ($x = 0.0, 0.2, 0.4, 0.6, 0.8, 1.0$) cathode materials for intermediate-temperature solid-oxide fuel cells, Ceram. Int. 40 (7) (2014) 11343–11350.

[21] L. Wang, R. Dou, M. Bai, Y. Li, D. Hall, Y. Chen, Characterisation of microstructure and hardness of perovskite-structured $Ba_{0.5}Sr_{0.5}Co_{0.8}Fe_{0.2}O_{3-\delta}$ under different sintering conditions, J. Eur. Ceram. Soc. 36 (7) (2016) 1659–1667.

[22] X.-B. Xie, Q. Xu, D.-P. Huang, J. Xiao, M. Chen, K. Zhao, D.-C. Chen, F. Zhang, An insight into the electrocatalytic properties of porous $La_{0.3}Sr_{0.7}Fe_{0.7}Cr_{0.3}O_{3-\delta}$ electrodes towards oxygen reduction reaction, J. Solid State Electrochem. 25 (3) (2021) 1007–1018.

[23] B. Molero-Sánchez, J. Prado-Gonjal, D. Ávila-Brande, M. Chen, E. Morán, V. Birss, High performance $La_{0.3}Ca_{0.7}Cr_{0.3}Fe_{0.7}O_{3-\delta}$ air electrode for reversible solid oxide fuel cell applications, Int. J. Hydrogen Energy 40 (4) (2015) 1902–1910.

[24] D.M. Bierschenk, J.M. Haag, K.R. Poeppelmeier, S.A. Barnett, Performance and stability of $LaSr_2Fe_2CrO_{9-\delta}$-Based solid oxide fuel cell anodes in hydrogen and carbon monoxide, J. Electrochem. Soc. 160 (2) (2012) F90–F93.

[25] B. Molero-Sánchez, P. Addo, M. Chen, S. Paulson, V. Birss, $La_{0.3}Ca_{0.7}Fe_{0.7}Cr_{0.3}O_{3-\delta}$ as a Novel Air Electrode Material for Solid Oxide Electrolysis Cells, 11th European SOFC & SOE FORUM 2014, 2014, p. B0804.

[26] P.K. Addo, B. Molero-Sanchez, A. Buyukaksoy, S. Paulson, V. Birss, Sulfur tolerance of $La_{0.3}M_{0.7}Fe_{0.7}Cr_{0.3}O_{3-d}$ (M= Sr, Ca) solid oxide fuel cell anodes, ECS Trans. 66 (2) (2015) 219–228.

[27] J.M. Haag, S.A. Barnett, J.W. Richardson Jr., K.R. Poeppelmeier, Structural and chemical evolution of the SOFC anode $La_{0.30}Sr_{0.70}Fe_{0.70}Cr_{0.30}O_{3-\delta}$ upon reduction and oxidation: an in situ neutron diffraction study, Chem. Mater. 22 (10) (2010) 3283–3289.

[28] P. Aguiar, E. Ramírez-Cabrera, N. Laosiripojana, A. Atkinson, L.S. Kershenbaum, D. Chadwick, Oxide catalysts in indirect internal steam reforming of methane in SOFC, in: M. Anpo, M. Onaka, H. Yamashita (Eds.), Studies in Surface Science and Catalysis, Elsevier, 2003, pp. 387–390. https://doi.org/10.1016/S0167-2991(03)80241-0.

[29] R.T. Baker, I.S. Metcalfe, P.H. Middleton, B.C.H. Steele, Evaluation of perovskite anodes for the complete oxidation of dry methane in solid oxide fuel cells, Solid State Ionics 72 (1994) 328–333.

[30] P.K. Addo, B. Molero-Sanchez, M. Chen, S. Paulson, V. Birss, CO/CO_2 study of high performance $La_{0.3}Sr_{0.7}Fe_{0.7}Cr_{0.3}O_{3-\delta}$ reversible SOFC electrodes, Fuel Cell. 15 (5) (2015) 689–696.

[31] X.-B. Xie, Q. Xu, J. Xiao, M. Chen, D.-C. Chen, D.-P. Huang, F. Zhang, Improved electrocatalytic properties of $La_{0.3}Ca_{0.7}Fe_{0.7}Cr_{0.3}O_{3-\delta}$ electrodes for oxygen reduction reaction: the effect of electrode thickness, Mater. Res. Bull. 131 (2020), 110967.

[32] V. Birss, B. Molero-Sanchez, P. Addo, M. Chen, High Performance Oxygen and Fuel Electrode for Reversible Solid Oxide Fuel Cell Applications, US Patent, 2018.

[33] B. Molero-Sánchez, J. Prado-Gonjal, D. Ávila-Brande, V. Birss, E. Morán, Microwave-assisted synthesis and characterization of new cathodic material for solid oxide fuel cells: $La_{0.3}Ca_{0.7}Fe_{0.7}Cr_{0.3}O_{3-\delta}$, Ceram. Int. 41 (7) (2015) 8411–8416.

[34] B. Molero-Sánchez, E. Morán, V. Birss, Rapid and low-energy fabrication of symmetrical solid oxide cells by microwave methods, ACS Omega 2 (7) (2017) 3716–3723.

[35] M.M. González-Barrios, M. Tabuyo-Martínez, V.C. Jiménez, Ó.J. Durá, J.A. Alonso, D. Ávila-Brande, J. Prado-Gonjal, Microwave-assisted synthesis of thermoelectric oxides and chalcogenides, Ceram. Int. (2022).

[36] J. Prado-Gonjal, R. Schmidt, D. Ávila, U. Amador, E. Morán, Structural and physical properties of microwave synthesized orthorhombic perovskite erbium chromite $ErCrO_3$, J. Eur. Ceram. Soc. 32 (3) (2012) 611–618.

[37] J. Jiang, Y. Long, X. Hu, J. Hu, M. Zhu, S. Zhou, A facile microwave-assisted synthesis of mesoporous hydroxyapatite as an efficient adsorbent for Pb^{2+} adsorption, J. Solid State Chem. 289 (2020), 121491.

[38] F. Murgia, P. Antitomaso, L. Stievano, L. Monconduit, R. Berthelot, Express and low-cost microwave synthesis of the ternary Chevrel phase $Cu_2Mo_6S_8$ for application in rechargeable magnesium batteries, J. Solid State Chem. 242 (2016) 151–154.

[39] K.J. Rao, B. Vaidhyanathan, M. Ganguli, P. Ramakrishnan, Synthesis of inorganic solids using microwaves, Chem. Mater. 11 (4) (1999) 882–895.

[40] J. Rodríguez-Carvajal, Recent advances in magnetic structure determination by neutron powder diffraction, Phys. B Condens. Matter 192 (1–2) (1993) 55–69.

[41] E. Bertaut, Magnetic structure analysis and group theory, J. Phys. Colloq. 32 (C1) (1971). C1-462-C1-470.

[42] D. Johnson, ZView: a Software Program for IES Analysis, 2002, 200, Version 2.

[43] J. Hudspeth, D. Goossens, A.J. Studer, R. Withers, L. Norén, The crystal and magnetic structures of $LaCa_2Fe_3O_8$ and $NdCa_2Fe_3O_8$, J. Phys. Condens. Matter 21 (12) (2009), 124206.

[44] E. Bertaut, P. Blum, A. Sagnieres, Structure du ferrite bicalcique et de la brownmillerite, Acta Crystallogr. 12 (2) (1959) 149–159.

[45] A. Varma, A.S. Mukasyan, A.S. Rogachev, K.V. Manukyan, Solution combustion synthesis of nanoscale materials, Chem. Rev. 116 (23) (2016) 14493–14586.

[46] J. Prado-Gonjal, R. Schmidt, J. Espíndola-Canuto, P. Ramos-Alvarez, E. Morán, Increased ionic conductivity in microwave hydrothermally synthesized rare-earth doped ceria $Ce_{1-x}RE_xO_{2-(x/2)}$, J. Power Sources 209 (2012) 163–171.

[47] R. Schmidt, Impedance spectroscopy of nanomaterials, in: B. Kharisov, O. Kharissova, U. Ortiz-Mendez (Eds.), CRC Concise Encyclopedia of Nanotechnology, CRC Press Taylor & Francis Group, Boca Raton (USA), 2015.

[48] J.T. Irvine, D.C. Sinclair, A.R. West, Electroceramics: characterization by impedance spectroscopy, Adv. Mater. 2 (3) (1990) 132–138.